Directionality Reversal and Shift of Rotational Axis in a Hemithioindigo Macrocyclic Molecular Motor

Lilli Reißenweber,[a] *Edgar Uhl,*[b] *Frank Hampel,*[a] *Peter Mayer,*[b] *Henry Dube*[a]*

[a] Friedrich-Alexander-Universität Erlangen-Nürnberg, Department of Chemistry and Pharmacy, Nikolaus-Fiebiger-Str. 10, 91058 Erlangen, Germany.

[b] Ludwig-Maximilians-Universität München, Department of Chemistry and Munich Center for Integrated Protein Science CIPSM, D-81377 Munich, Germany.

* E-mail: henry.dube@fau.de

Abstract

Molecular motors are central driving units for nanomachinery and control of their directional motions is of fundamental importance for their functions. Light-driven variants use an easy to provide, easy to dose, and waste free fuel with high energy content, making them particularly interesting for applications. Typically, light-driven molecular motors work *via* rotations around dedicated chemical bonds where directionality of the rotation is dictated by the steric effects of asymmetry in close vicinity to the rotation axis. In this work we show how unidirectional rotation around a virtual axis can be realized by reprogramming a molecular motor. To this end, a classical light-driven motor is restricted by macrocyclization and its intrinsic directional rotation is transformed into a directional rotation of the macrocyclic chain in the opposite direction. Further, solvent polarity changes allow to toggle the function of this molecular machine between a directional motor and a non-directional photoswitch. In this way a new concept for the design of molecular motors is delivered together with elaborate control over their motions and functions by simple solvent changes. The possibility of sensing the environmental polarity and correspondingly adjusting directionality of motions opens up a next level of control and responsiveness to light-driven nanoscopic motors.

https://doi.org/10.26434/chemrxiv-2024-6f898 **ORCID:** https://orcid.org/0000-0002-5055-9924 Content not peer-reviewed by ChemRxiv. **License:** CC BY 4.0

Introduction

Artificial molecular machines are miniaturized versions of macroscopic machines and work by controlling dedicated motions within their molecular structures.[1-9] Such control needs to be achieved against the equilibrating force of the *Brownian* motion to allow operation out of equilibrium.[10, 11] In this regard molecular motors stand out as one of the most important sub-types of molecular machines as they convert external energy input into directional motions, which are not canceling out over continuous operation.[2, 5, 12-17] The first realization of a molecular motor was achieved in 1999 by *Feringa*, who used the light-driven double bond isomerization of an overcrowded stilbene as energy fueling mechanism.[18] This achievement gave rise inter alia to the *Nobel* prize in chemistry in 2016.[3] Since then, the development of molecular motors is growing ever steeply and today a large number of different variants with different working mechanisms, energy supplies, and types of motions are available. They include catenane based structures as first developed by *Leigh*, where rotation of one macrocyclic ring around another proceeds directionally (for selected examples see [19-21]), chemically driven variants rotating around a single bond[22] as pioneered again by *Feringa*,[23, 24] surface bound structures rotating around an axis perpendicular to the surface and energized by electric current,[25, 26] or just recently added electrically driven versions in solution.[27] Further examples include linear molecular motors such as walkers[28, 29] and pumps,[30-36] which use distinct mechanisms and fuels to achieve a directional linear motion. When it comes to fueling however, simple illumination is particularly attractive because energy can be supplied continuously and precisely dosed, no waste is accumulated during operation, and the energy content of photons is very high. To date, a number of light-driven rotary motor types has been introduced, most eminently overcrowded alkenes from the *Feringa* group,[18, 37, 38] imine-based motors from *Greb* and *Lehn*,[39, 40] and hemithioindigo (HTI)-based systems from our group.[41-48] More recent additions to light-driven molecular motors inherit biomimetic chromophores[49] or heterocyclic alkenes.[50, 51] Currently, incorporation of light driven molecular motors into larger molecular setups is pursued in order to utilize the work that they can produce and to fulfill a specific task.[52] In this context the active disentanglement of polymer strands,[53, 54] transmission of motor rotation to remote entities,[55] active acceleration of remote passive rotary motions,[56] controlled motor motion restrictions,[57] or energy storage and subsequent triggered reverse motor rotation[58] represent important steps to realize the full potential of molecular motors for driving advanced nanomachinery. Furthermore, disentanglement by molecular motors can be used to shift coupled chemical equilibria in response to strain[59] and motor-powered active molecular threading allows to

https://doi.org/10.26434/chemrxiv-2024-6f898 **ORCID:** https://orcid.org/0000-0002-5055-9924 Content not peer-reviewed by ChemRxiv. **License:** CC BY 4.0

repeatedly move a molecular string through a macrocycle – a process akin to macroscopic sewing or weaving.[60] The utility of macrocyclization was further employed by our group to evidence unidirectionality in ultra-fast molecular rotary motors in a photochemical way.[61] In larger macrocyclic setups it even becomes possible to control multiple types of motions, such as 360° motor rotation, 180° biaryl rotations, and structural reconfigurations, within the same molecular machine with very high precision.[62] However, in virtually all of these motor systems, a defined chemical bond (double or single bond) represents the actual rotational axis. Light-driven molecular motors possessing a different molecular axis remain an exception so far. In this context, *Haberhauer* introduced a multi-stimuli molecular motor based on an azobenzene photoswitch connected to a chiral bipyridine clamp.[63] The seminal photon-only molecular motor from our group can be regarded as another example for providing a directional rotation around a virtual axis.[44]

In this work we present a different concept to establish directional light-driven motor rotations around a virtual axis. To this end we reprogram the directional rotations of a "classical" HTI-molecular motor[41] by aid of a constricting macrocycle (Figure 1). In this minimal macrocyclic system, the inherent 360° unidirectional rotation around the double bond axis of the motor is restricted to only 180° within one molecular half-space. However, *E*/*Z* and *Z*/*E* photoisomerization reactions are thermally ratcheted by intervening atropisomerization reactions, which break symmetry and thus give rise to a resulting unidirectional motion of the macrocyclic linker chain around a virtual axis. As a result, the rotation direction of this macrocyclic motor is not only shifted by about 60° but the rotation direction itself is reversed with respect to the intrinsic rotation direction of the double bond axis. With this concept it is shown how directional molecular rotations can be realized in a completely different way by transforming and restricting the inherent directional motion of a light-driven motor. Further, the resulting four-step motor shows a strong dependence of state stabilities on solvent polarity. Because of this dependence, simple solvent changes transform the molecular motor into a molecular photoswitch and vice versa, giving rise to another level of outside control over the function of this machine. In principle this property can be used deliberately to sense the polarity of the environment in which the machine is working and respond to that environment with a specific function (motor versus switch motions).

https://doi.org/10.26434/chemrxiv-2024-6f898 **ORCID:** https://orcid.org/0000-0002-5055-9924 Content not peer-reviewed by ChemRxiv. **License:** CC BY 4.0

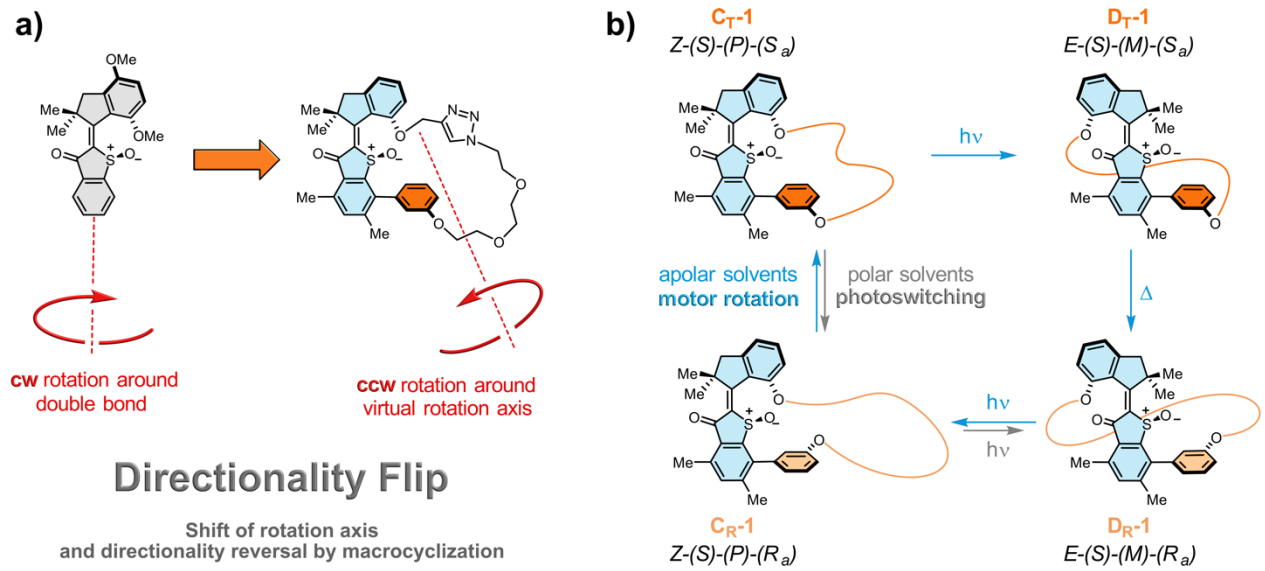

Figure 1 *Shift of rotational axis and reversal of molecular motor directionality by macrocyclization. a) Clockwise (cw) rotation of the classical HTI motor. Macrocyclization and introduction of a biaryl unit in ortho-position at the thioindigo fragment leads to counterclockwise (ccw) rotation around a virtual rotational axis. b) Rotational cycle of macrocyclic molecular motor **1**. Alternating double bond photoisomerization and thermal atropisomerization processes furnish a ccw rotation of the PEG-linker chain around a virtual rotational axis. By changing the solvent polarity, the motor can be transformed into a molecular photoswitch.*

Results and Discussion

Macrocyclic system **1** was synthesized using an approach similar to a previously published procedure for macrocyclic motors (Figure 2a).[56] However, different to earlier macrocyclic motors from our group, motor **1** incorporates the asymmetric biaryl moiety in *ortho*-position to the sulfur atom, which gives rise to a 90° angle of the biaryl axis with respect to the photoisomerizable double bond. Introduction of the bromide at this position in the precursor HTI was achieved by an unexpected halogen migration from *para*- to *ortho*-position during the intramolecular *Friedel-Crafts* acylation of precursor **2**. The resulting benzothiophenone **3** was condensed with indanone **4** to form the corresponding brominated HTI **5**. After attachment of a short polyethylene glycol (PEG) chain **6** *via* an azide-alkyne *Huisgen* click-reaction to yield **7**, an intramolecular *Suzuki* cross-coupling leads to the macrocyclized HTI **8**. Final oxidation of the sulfur to the corresponding sulfoxide **1** introduces the chiral information necessary for unidirectional motor rotation. With oxidation of the sulfur, two molecular half-spaces are established relative to the position of the

https://doi.org/10.26434/chemrxiv-2024-6f898 **ORCID:** https://orcid.org/0000-0002-5055-9924 Content not peer-reviewed by ChemRxiv. **License:** CC BY 4.0

sulfoxide oxygen with respect to the plane of the thioindigo fragment. We arbitrarily termed the half space containing the sulfoxide oxygen as top half-space and the opposite as bottom half-space (Figure 2b). For detailed synthetic information see the Supporting Information chapter 2.

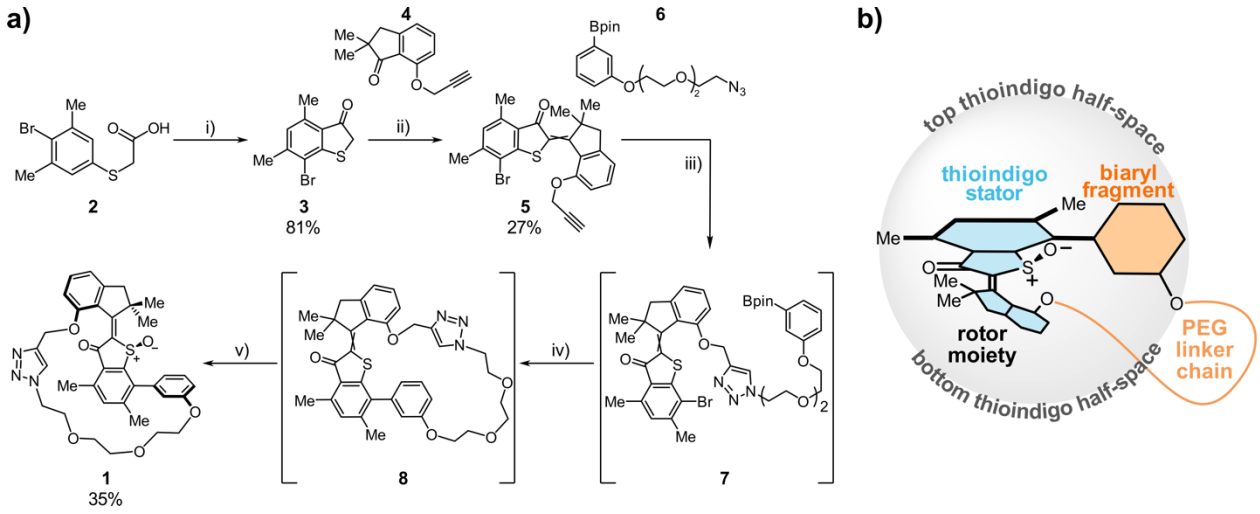

Figure 2 *a) Synthesis of macrocyclic molecular motor **1**. i) 1. Thionyl chloride, reflux, 1.5 h, 2. Aluminum(III)chloride (3.0 eq.), CH_2Cl_2, 0 °C to 23 °C, 2 h. ii) Boron trichloride, CH_2Cl_2, –78 °C to 0 °C, 10 min. iii) Sodium ascorbate, $CuSO_4 \cdot 5H_2O$, DMF, 23 °C, 3 d. iv) K_2CO_3, $Pd(PPh_3)_4$, H_2O, DMF, 85 °C, 20 h. v) $NaBO_3 \cdot 4H_2O$, acetic acid, 23 °C, 5 h. b) Schematic representation of macrocyclic motor system **1** and explanation of the terminology used to describe its different molecular fragments and the molecular half-spaces.*

Taking together all stereo-elements present in **1**, eight diastereomers are possible for one configuration of the sulfoxide stereo-center (Figure 3a). For simplicity only (*S*)-configured sulfoxide structures are shown and discussed in the following. The isomers are termed **A**, **B**, **C**, and **D** with corresponding subscripts **R** and **T** referring to a relaxed or tense arrangement of the PEG-chain within the macrocycle. Six of the eight possible isomers were observed directly experimentally by different techniques. Single crystals suitable for X-ray structural analysis could be obtained for the four isomers $\mathbf{A_R}$-**1**, $\mathbf{B_R}$-**1**, $\mathbf{C_R}$-**1**, and $\mathbf{D_R}$-**1** (Figure 3b). Isomers $\mathbf{C_T}$-**1** and $\mathbf{D_T}$-**1** were obtained in solution experiments. Two isomers, $\mathbf{A_T}$-**1** and $\mathbf{B_T}$-**1**, were not observed to be populated because they would require an unfavorable helix conformation in conjunction with substantial strain in the short PEG-linker chain. Detailed information on the assignments of the

https://doi.org/10.26434/chemrxiv-2024-6f898 **ORCID:** https://orcid.org/0000-0002-5055-9924 Content not peer-reviewed by ChemRxiv. **License:** CC BY 4.0

different isomers and their structural elucidation can be found below and in the Supporting Information.

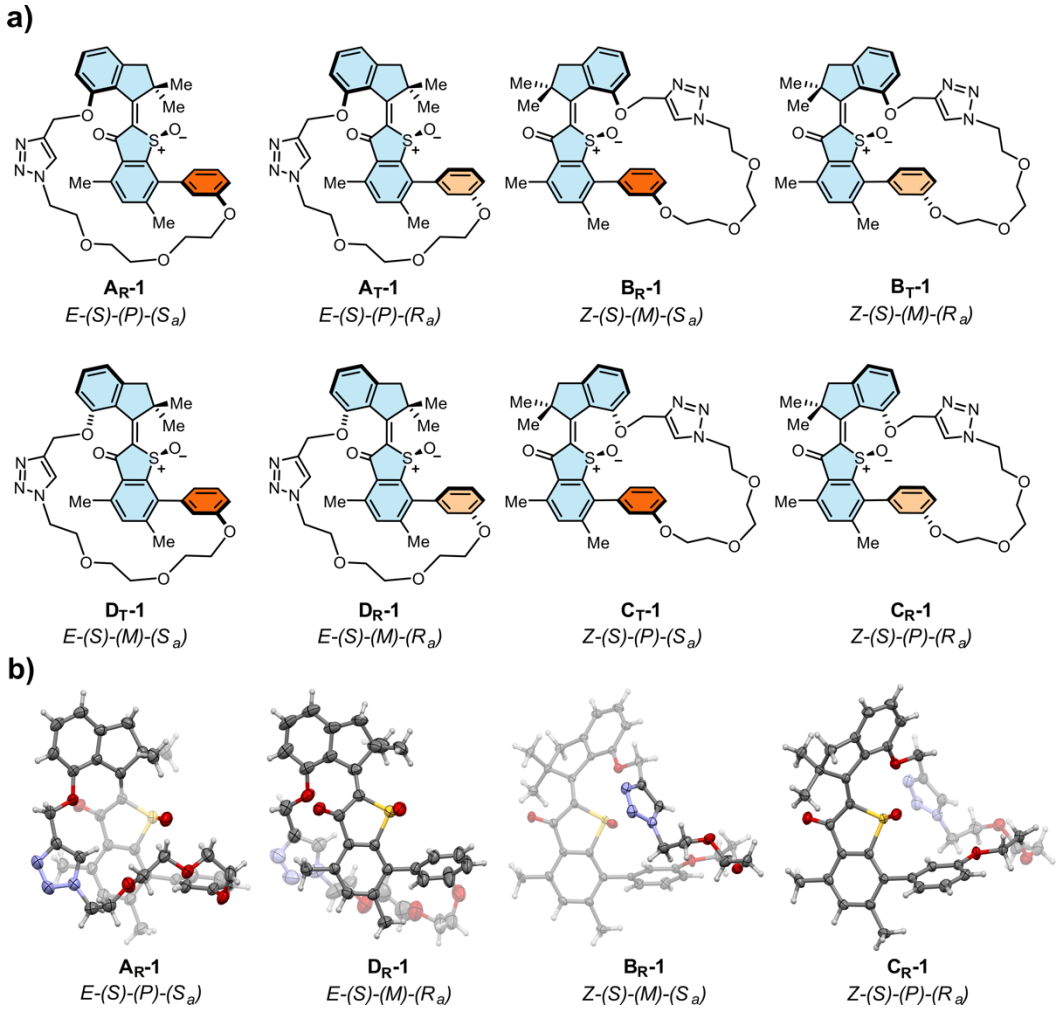

Figure 3 *a) Schematic representation of all possible diastereomeric isomers of motor system **1**. Only the (S)-configured enantiomers are shown for clarity. The biaryl unit is colored in dark orange for (S_a)-configured atropisomers and in light orange for (R_a)-configurations. b) Crystal structures of racemic isomers **A_R-1** E-(S)-(P)-(S_a), **D_R-1** E-(S)-(M)-(R_a), **B_R-1** Z-(S)-(M)-(S_a) and **C_R-1** Z-(S)-(P)-(R_a) with 50% probability ellipsoids.*

A comprehensive theoretical analysis was conducted for macrocyclic motor **1** on the ωB97xD/6-311++ G(d,p) IEPPCM (CH_2Cl_2 or CS_2) level of theory (Figure 4) in order to establish the energy landscape in the ground state, the different stabilities of isomeric states and their molecular structures, as well as the corresponding spectral signatures (see Supporting Information chapter 8 for details). As isomer **A_R-1** was obtained from the synthesis as one main product and

https://doi.org/10.26434/chemrxiv-2024-6f898 **ORCID:** https://orcid.org/0000-0002-5055-9924 Content not peer-reviewed by ChemRxiv. **License:** CC BY 4.0

then was found to convert irreversibly with light first into **B$_R$-1** and ultimately into **C**-and **D**-type isomers, **A$_R$-1** and **B$_R$-1** were also included in the energy scheme shown in Figure 4. However, once **C**-and **D**-type isomers are populated, light induced photoisomerizations and thermal atropisomerization reactions only lead to conversions between isomers **C$_R$-1**, **C$_T$-1**, **D$_R$-1**, and **D$_T$-1**. In the following we therefore focus on the latter four isomers and their properties.

The calculated energy scheme for the **C**-and **D**-type isomers shows that three isomers **C$_R$-1**, **C$_T$-1**, and **D$_R$-1** represent the most stable structures with isomer **C$_T$-1** as the global minimum. **C$_T$-1** possesses *Z*-configuration of the photoisomerizable double bond, an energetically favorable (*P*)-helicity, and a (S_a)-configured biaryl axis. This stereo-configuration forces the PEG-linker chain to be in a tensed state (**T**) as its attachment points at the rotor and the biaryl fragments are residing in opposite half-spaces with respect to the thioindigo-fragment plane (see also Figure 2b for definitions of molecular fragments and half-spaces). The **C$_R$-1** isomer has the same stereo-configuration except for the axial chirality of the biaryl, which is (R_a)-configured in this case. As a result, the PEG-linker chain is in the relaxed state (**R**) in this isomer, which makes it in fact the expected global minimum. However, the calculated energy difference between **C$_R$-1** and **C$_T$-1** is only 2.2 kcal/mol, which lies within the typical error for DFT calculations. For this reason, it can be assumed that both isomers **C$_R$-1** and **C$_T$-1** are rather similar in energy and could both be populated. Furthermore, the exact energy differences are subject to change when including different solvent models in the calculations. If an apolar solvent model like CS_2 is included, isomer **C$_T$-1** is stabilized versus **C$_R$-1**, while a polar solvent model increases the stability of **C$_R$-1**. This is exactly observed in the experiments where the energetic order of **C$_R$-1** and **C$_T$-1** can actually be completely inverted, which enables solvent induced reversible toggling between motor and photoswitch functions. The **D$_R$-1** isomer possesses *E*-configuration of the double bond, a less favorable (*M*)-helicity, and a (R_a)-configured biaryl axis leading to a relaxed (**R**) PEG-chain. The **D$_T$-1** isomer inherits *E*-(*M*)-(S_a) configuration and thus a tense (**T**) PEG-chain. Again, a rather small energy difference of 1.8 kcal/mol is found theoretically between the more stable **D$_R$-1** and the less stable **D$_T$-1** isomer. The calculated order of stability is however fully supported by the experiments where a complete thermal conversion from **D$_T$-1** to **D$_R$-1** occurs regardless of solvent polarity changes.

When taking into account the calculated energies of the **C**-and **D**-type isomers, a four-step cycle of sequential interconversions can be established. Starting from the global minimum **C$_T$-1** isomer, light irradiation induces *Z* to *E* photoisomerization to populate **D$_T$-1** without changing axial

https://doi.org/10.26434/chemrxiv-2024-6f898 **ORCID:** https://orcid.org/0000-0002-5055-9924 Content not peer-reviewed by ChemRxiv. **License:** CC BY 4.0

chirality of the biaryl. Isomer $\mathbf{D_T}$-**1** is highly metastable and releases tension of the PEG-linker chain in a thermal atropisomerization step leading to population of $\mathbf{D_R}$-**1**. This step can be regarded as a thermal ratcheting step, effectively removing population from the $\mathbf{C_T}$-**1**/$\mathbf{D_T}$-**1** photoequilibrium. A second light irradiation induces *E* to *Z* photoisomerization of $\mathbf{D_R}$-**1** to populate $\mathbf{C_R}$-**1**, again without changing axial chirality of the biaryl axis. A final thermal atropisomerization inverts the biaryl axial chirality yielding again the $\mathbf{C_T}$-**1** isomer. At this point it should be noted that if the energy order between $\mathbf{C_R}$-**1** and $\mathbf{C_T}$-**1** is inverted, the four-step cycle is halted and only back-and-forth photoswitching between $\mathbf{C_R}$-**1** and $\mathbf{D_R}$-**1** is taking place. The reason for this behavior is that these two isomers now represent the most stable *E* and *Z* isomeric forms of **1** and no thermal ratcheting steps are taking place to shift populations to another photoequilibrium.

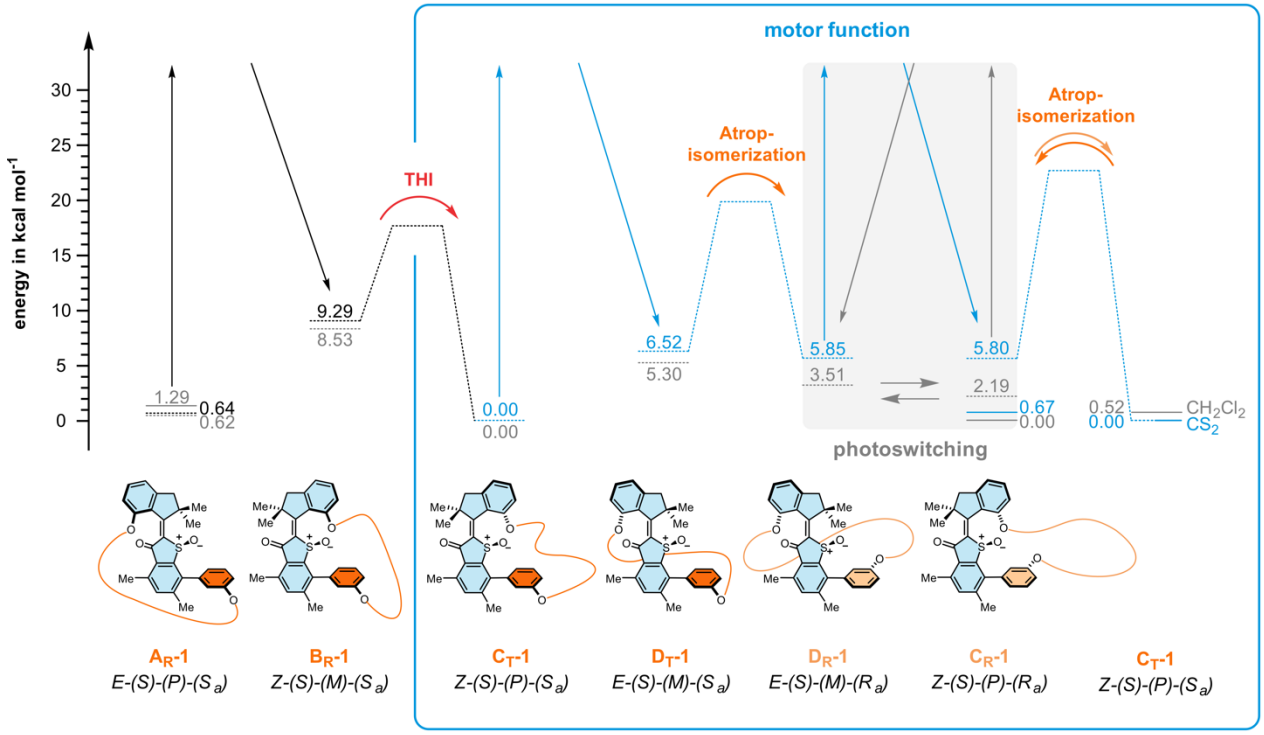

Figure 4 *Theoretical ground-state energy profile of macrocyclic molecular motor* ***1*** *calculated at the ωB97xd/6-311++G(d,p) IEFPCM(CH_2Cl_2 or CS_2) level of theory (black, blue and grey dashed) and corresponding experimental values (blue and grey solid). Schematic representations of the six populated states with different stereochemical configurations are shown. For detailed information and calculated structures see Supporting Information chapter 8. Despite six isomers being accessible, the actual motor rotational cycle of* ***1*** *starts from isomer* $\boldsymbol{C_T}$***-1*** *which undergoes a sequence of light induced double bond isomerization and atropisomerization processes (blue box). Solvent induced inversion of* $\boldsymbol{C_T}$***-1*** *and* $\boldsymbol{C_R}$***-1*** *stability leads to toggling between four-step motor*

https://doi.org/10.26434/chemrxiv-2024-6f898 **ORCID:** https://orcid.org/0000-0002-5055-9924 Content not peer-reviewed by ChemRxiv. **License:** CC BY 4.0

*function in apolar solvents like CS_2 and sole photoswitching between **D_R-1** and **C_R-1** (grey area)) in polar solvents like CH_2Cl_2.*

With aid of the theoretical description, experimental characterization and elucidation of the working mechanism of molecular machine **1** was undertaken next. The **A_R-1** isomer and a mixture of **C_T-1** and **C_R-1** could be obtained separately from the synthesis. X-ray crystallographic analysis of **A_R-1** directly revealed *E*-(*S*)-(*P*)-(S_a) configuration of this isomer with the PEG-chain residing in the same half-space as the chiral sulfoxide oxygen atom (Figure 2b and 3b). Accordingly, solution NMR, UV/Vis, and electronic circular dichroism (ECD) spectra of **A_R-1** could unambiguously be assigned. The experimental spectra match very well with the theoretically predicted UV/Vis and ECD spectra lending further support for the assignment. Isomers **C_R-1** and **C_T-1** interconvert rapidly at ambient temperature prohibiting their separation by HPLC methods. They were therefore analyzed as mixtures in solution. However, we found that it is possible to strongly enrich each isomer **C_R-1** or **C_T-1** by choosing either polar or apolar solvents, respectively (Figure 5d-e, Figure 6e). In polar CH_2Cl_2 solution **C_R-1** is enriched in up to 71% and crystals suitable for X-ray analysis unambiguously evidenced *Z*-(*S*)-(*P*)-(R_a) configuration of this isomer (Figure 3b and 5c). In apolar CS_2 solution the **C**-isomeric mixture is strongly enriched in the **C_T-1** isomer in up to 76% (also see the Supporting Information chapter 4 for additional solvent screens). From that apolar solution co-crystals of **C_R-1** with **B_R-1** (with *Z*-(*S*)-(*M*)-(S_a) configuration) were formed instead of the expected **C_T-1** isomer as revealed by X-ray structural analysis (Figure 3b). However, the *Z*-(*S*)-(*M*)-(S_a) configuration of **B_R-1** proved already that the second isomer enriched in apolar solution inherits the same double bond configuration and opposite axial chirality of the biaryl moiety as compared to **C_R-1**. These two structural features are indeed the ones expected for isomer **C_T-1**. Only the (*M*)-helicity found in the co-crystal was not matching the expected more stable (*P*)-helicity of **C_T-1** leading to the presence of **B_R-1** instead. This unexpected capture of the instable helix in the condensed phase is most likely the result of crystal packing effects in the co-crystal, which leads to a nearly perfect structural overlap between **C_R-1** and **B_R-1** in the solid state (see details of the co-crystal elucidation in the Supporting Information). Thermal helix inversion is a highly dynamic process and thus is not inhibited kinetically if the higher energy of the unfavorable helix can be compensated. Indeed, when spectroscopically analyzing the corresponding solution mixture it became evident that in solution the second isomer is in fact **C_T-1** and not **B_R-1** because of the much more stable (*P*)-helicity of the former. To this end, NMR,

https://doi.org/10.26434/chemrxiv-2024-6f898 **ORCID:** https://orcid.org/0000-0002-5055-9924 Content not peer-reviewed by ChemRxiv. **License:** CC BY 4.0

UV/Vis, and especially ECD spectroscopy together with theoretical analysis allowed us to unambiguously identify the expected *Z*-(*S*)-(*P*)-(S_a) configuration of **C_T-1** for the isomer strongly enriched in apolar solvents (Figure 5). First, a clear identification of double bond and atropisomer configuration was achieved using Nuclear *Overhauser* effect (NOE) NMR spectroscopy (Figure 5f). Close proximity between the triazole proton 31 and the isolated biaryl proton 24 confirmed *Z* configuration of isomer **C_R-1** and residing of the biaryl-oxygen atom within the same molecular half-space as the sulfoxide oxygen atom, i.e. (R_a)-configuration of the biaryl axis. Correspondingly, proximity of triazole proton 31 to the opposite facing biaryl protons 20 and 22 evidenced *Z* configuration of the double bond and (S_a)-configuration of the axially chiral biaryl within **C_T-1**. Second, ECD spectroscopy allowed to directly probe helicity of the scrutinized isomer, which is opposite for **C_T-1** and **B_R-1**. The experimentally observed ECD spectra clearly show that helicity of the scrutinized isomer is the same as for **C_R-1**, which is manifest in the overall very similar ECD spectrum and *Cotton*-effect features (Figure 5d). Further, the corresponding calculated ECD spectra are in very close agreement with the experimental ones for both, **C_T-1** and **C_R-1**. They are exact enough to distinguish these two isomers, which are only differing in their axial chirality of the biaryl moiety as manifested in the Cotton-effect features between 250 nm and 300 nm (Figure 5d). The inverted helicity of isomer **B_R-1** expectedly leads to opposite Cotton-effects especially in the visible region of the calculated ECD spectrum, which does not match at all with the experimentally observed spectrum of the isomer enriched in apolar solvents (Figure 5e). Thus, this isomer could unambiguously be assigned to the **C_T-1** isomer by the comprehensive spectroscopy analysis.

Additionally, isomers **D_T-1** and **D_R-1** were obtained from irradiation experiments of the initial three isomers **A_R-1**, **C_T-1**, and **C_R-1**. Isomer **D_R-1** could be separated by HPLC at ambient temperatures enabling X-ray crystallographic analysis (Figure 3b) in combination with solution NOE NMR experiments. These experiments directly revealed *E*-(*S*)-(*M*)-(R_a) conformation of the **D_R-1** isomer. **D_T-1** was only observed at low temperatures (below –70 °C), however NOE NMR spectroscopy established *E*-configuration of the central double bond and a (S_a)-isomeric biaryl unit, which allowed an unambiguous assignment of this structure as well (see Supporting Information chapter 3.2.4 for the detailed analysis).

https://doi.org/10.26434/chemrxiv-2024-6f898 **ORCID:** https://orcid.org/0000-0002-5055-9924 Content not peer-reviewed by ChemRxiv. **License:** CC BY 4.0

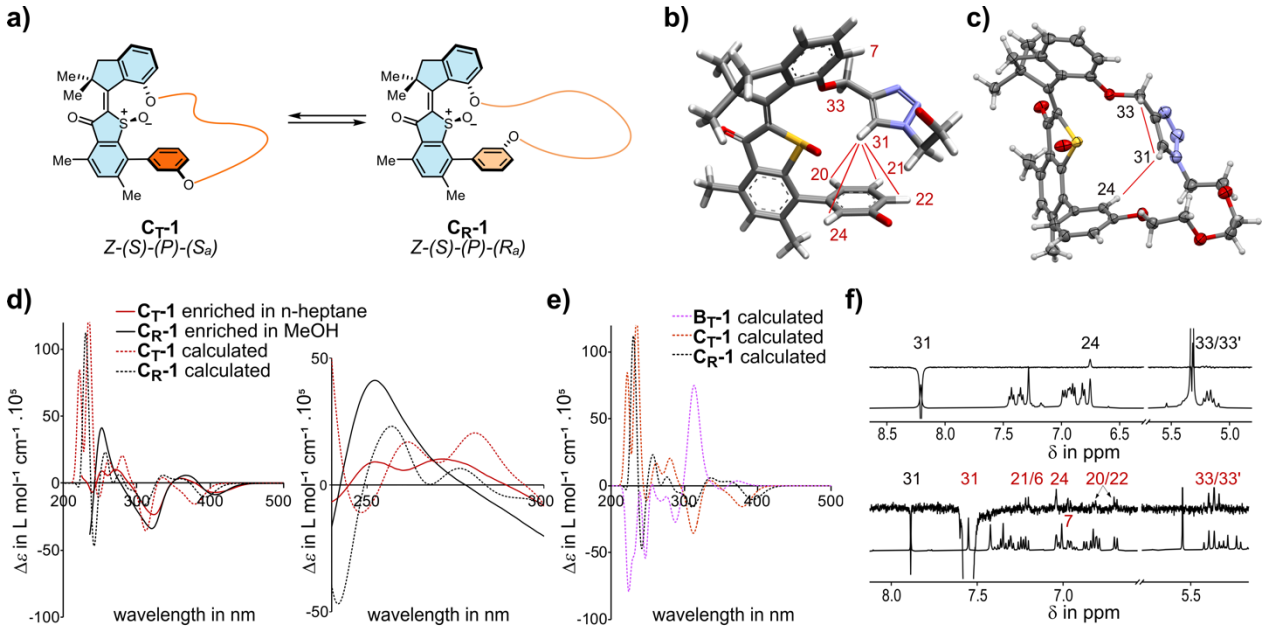

Figure 5 *Elucidation of **C_T-1** and **C_R-1** in solution. a) Schematic representation of the **C_T-1** to **C_R-1** interconversion via atropisomerization of the biaryl fragment. b) Excerpt of the theoretically obtained structure of **C_T-1** at the ωB97xD/6-311++G(d,p) IEFPCM (CH_2Cl_2) level of theory. c) Side view of the **C_R-1** structure in the crystalline state. d) Left: Experimental ECD spectra of a **C_T-1** enriched solution in n-heptane (red solid line) and a **C_R-1** enriched solution in methanol (black solid line). Right: Excerpt of the spectrum from 240 nm to 300 nm. Theoretically obtained spectra of **C_T-1** (dashed red line) and **C_R-1** (dashed black line) were redshifted by 27 nm. e) Theoretical ECD spectra of **B_T-1** (purple dashed line), **C_T-1** (red dashed line) and **C_R-1** (black dashed line) calculated at the ωB97xD/6-311++ G(d,p) IEFPCM(CH_2Cl_2) level of theory were redshifted by 27 nm. f) Top: ^{1}H ROE NMR spectrum (CD_2Cl_2, 400 MHz, –90 °C) of a mixture of **C_R-1** (83%) and **C_T-1** (17%) when irradiated at the resonance frequency of triazole proton 31 of major isomer **C_R-1**. Selective polarization transfer solely to aromatic proton 24 evidences (R_a)-configuration of the biaryl unit. Bottom: ^{1}H NOE NMR spectrum (THF-d_8:n-heptane = 2:1, 500 MHz, –20 °C) of **C_R-1** (37%) and **C_T-1** (73%) when irradiated at the resonance frequency of proton 31 of major isomer **C_T-1**. Polarization transfer to protons 20/22 evidences (S_a)-configuration of the biaryl unit.*

Isomers **A_R-1**, **C_T-1** and **C_R-1** as well as **D_R-1** could be used directly as starting points for thermal and photoirradiation experiments to decipher the function and working mechanism of **1**. Heating a solution of **A_R-1** to 120 °C in $(CDCl_2)_2$ led to population of **C_T-1** and **C_R-1** until an equilibrium distribution with 12% **A_R-1**, 19% **C_T-1**, and 69% **C_R-1** was established. This distribution could directly be translated into the relative free energy differences of the three isomers. Thus, the global

https://doi.org/10.26434/chemrxiv-2024-6f898 **ORCID:** https://orcid.org/0000-0002-5055-9924 Content not peer-reviewed by ChemRxiv. **License:** CC BY 4.0

minimum in this solvent was found to be **C$_R$-1**, followed by **C$_T$-1** (1.0 kcal·mol^{-1} higher in energy), and then **A$_R$-1** (1.3 kcal·mol^{-1} higher in energy). Analysis of the corresponding kinetic measurements using *COPASI*[64] revealed the *Gibbs* energies of activation, i.e. $\Delta G^{\neq}$ = 29.09 kcal·mol^{-1} for **A$_R$-1** to **C$_T$-1** isomerization at 120 °C and $\Delta G^{\neq}$ = 17.56 kcal·mol^{-1} for the **C$_T$-1** to **C$_R$-1** conversion at the same temperature. Heating **D$_R$-1** did not result in any population of **A$_R$-1**. Instead, thermal conversion of **D$_R$-1** to **C$_R$-1** with a corresponding $\Delta G^{\neq}$ = 22.58 kcal·mol^{-1} and subsequent **C$_R$-1** and **C$_T$-1** equilibration is observed at 40 °C in $(CDCl_2)_2$. These findings excluded thermally induced helix inversion and atropisomerization of the biaryl moiety in **D$_R$-1**, which would be accompanied by the ethylene glycol chain moving from one half-space of the thioindigo fragment plane to the other. Therefore, no 360° rotation around the central double bond is possible in machine **1** via thermally activated processes.

At ambient temperatures irradiation of *E*-isomeric **A$_R$-1** with 470 nm light leads to a photostationary state (pss) with the isomer composition 17% **C$_T$-1**, 44% **C$_R$-1**, and 39% **D$_R$-1**. No residual isomer **A$_R$-1** remains and **A$_R$-1** also cannot be repopulated at any other wavelength of irradiation tested (see the Supporting Information chapter 6.1 for details). This experiment shows directly that **A$_R$-1** only serves as entry point for reaching the actual working mechanism of this molecular machine. Cooling **A$_R$-1** to –90 °C in CD_2Cl_2 solution and subsequent *in situ* irradiation in the NMR spectrometer revealed a more detailed picture. At the lower temperature, photo-induced interconversion of **A$_R$-1** to *Z*-configured **C$_T$-1** is observed, which possesses the same (S_a) axial chirality. As is the case for related HTI-motors, the direct photoproduct of **A$_R$-1**, i.e. **B$_R$-1**, remained elusive in solution and was not observed even at –108 °C because of its very fast thermal helix inversion (THI) immediately forming **C$_T$-1**. After accumulation of **C$_T$-1** and switching off the light, warming the mixture to –70 °C induced thermal atropisomerization of the biaryl moiety in **C$_T$-1** and population of only isomer **C$_R$-1**. A *Gibbs* free energy of activation of $\Delta G^{\neq}$ = 15.54 kcal·mol^{-1} was measured for this process (see the Supporting Information chapter 6.2.3). If instead, irradiation was continued at –90 °C two more intermediate states, i.e. **D$_T$-1** and **D$_R$-1**, were observed to be populated in sequence. In order to disentangle the multiple isomer interconversions additional experiments were conducted at –108 °C in a 1:3 mixture of CD_2Cl_2:CS_2. At this low temperature irradiation of *E*-isomeric **A$_R$-1** first populated *Z*-isomeric **C$_T$-1** (via elusive **B$_R$-1**), which photoisomerized further to form exclusively *E*-isomeric **D$_T$-1** (Figure 6a). In this sequence of isomer interconversions, the same (*S*a)-configuration of the biaryl axis is

https://doi.org/10.26434/chemrxiv-2024-6f898 **ORCID:** https://orcid.org/0000-0002-5055-9924 Content not peer-reviewed by ChemRxiv. **License:** CC BY 4.0

retained. Isomer $\mathbf{D_T}$**-1** was then scrutinized for its thermally induced motions in CD_2Cl_2 solution at –90 °C, which revealed exclusive and complete thermal atropisomerization populating only $\mathbf{D_R}$**-1** (Figure 6b). Kinetic analysis of this process corresponded to an energy barrier of $\Delta G^{\neq} = 13.11$ kcal·mol^{-1}. When irradiating a solution of pure $\mathbf{D_R}$**-1** at –90 °C in CD_2Cl_2 solution, only light induced photoisomerization to *Z*-isomeric $\mathbf{C_R}$**-1** was observed establishing a photoequilibrium between just these two isomers (Figure 6c). Allowing the sample to warm to 25 °C resulted in thermal conversion of $\mathbf{C_R}$**-1** to $\mathbf{C_T}$**-1** in up to 22% (Figure 6d) via a thermally activated atropisomerization of the biaryl moiety. Although $\mathbf{C_R}$**-1** is still the dominant isomer in the final mixture in polar CD_2Cl_2 solution, this last transformation directly evidences completion of a four-step interconversion cycle. When moving to an apolar solvent like CS_2 the relative stability of $\mathbf{C_R}$**-1** to $\mathbf{C_T}$**-1** is inverted and $\mathbf{C_T}$**-1** becomes the dominant isomer in up to 73% (Figure 6e). In this case the last thermal atropisomerization step also becomes dominant and so does the entire four-step cycle.

Taken together, this behavior establishes a continuous four-step cycle of isomer interconversions under continued illumination in apolar solvents. The cycle proceeds via an initial double bond photoisomerization from $\mathbf{C_T}$**-1** to $\mathbf{D_T}$**-1** followed by a thermal atropisomerization ratcheting step from $\mathbf{D_T}$**-1** to $\mathbf{D_R}$**-1**, photoisomerization from $\mathbf{D_R}$**-1** to $\mathbf{C_R}$**-1**, and a final thermal atropisomerization from $\mathbf{C_R}$**-1** to $\mathbf{C_T}$**-1**. It needs to be emphasized here that the two thermal atropisomerization steps are proceeding with significantly different efficiencies. While $\mathbf{D_T}$**-1** to $\mathbf{D_R}$**-1** conversion is quantitative, the conversion from $\mathbf{C_R}$**-1** to $\mathbf{C_T}$**-1** strongly depends on the relative energies of these two states, which can be switched upside down by choice of the solvent (Figure 6e). Therefore, a proficient four-step cycle is present in apolar solvents such as CS_2, whereas in polar solvents like CD_2Cl_2 the dominating process is simple photoswitching between $\mathbf{C_R}$**-1** and $\mathbf{D_R}$**-1**. A related toggling between switch and motor function reported earlier required much more drastic chemical changes, i.e. acid base additions to a dedicated basic site of the motor.[65]

Isomer $\mathbf{A_R}$**-1** was not found to be populated under any illumination conditions, which also excludes a light-induced 360° rotation around the central double bond in machine **1** (see the Supporting Information chapter 6.1).

https://doi.org/10.26434/chemrxiv-2024-6f898 **ORCID:** https://orcid.org/0000-0002-5055-9924 Content not peer-reviewed by ChemRxiv. **License:** CC BY 4.0

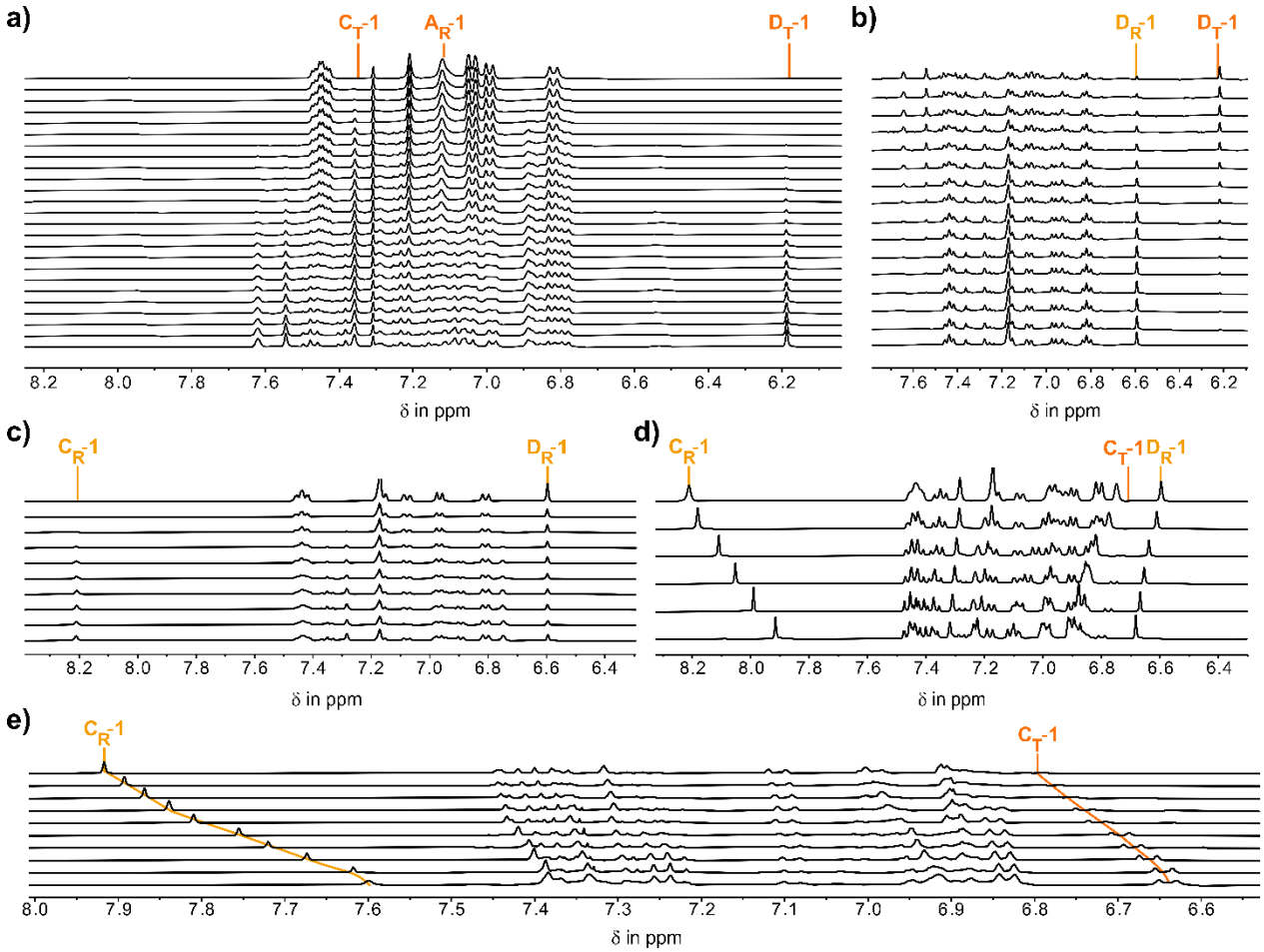

Figure 6 *Experimental elucidation of the isomer interconversions of macrocycle* ***1****. a)* ^{1}*H NMR spectra (*CD_2Cl_2*:*CS_2* = 1:3, 400 MHz, –108 °C) recorded while irradiating initially pure isomer* ***A*****$_R$****-1 with 470 nm light, which leads to population of* ***C*****$_T$****-1 and subsequent accumulation of* ***D*****$_T$****-1. b)* ^{1}*H NMR spectra (*CD_2Cl_2*, 400 MHz, –90 °C) following the thermal decay of* ***D*****$_T$****-1 to* ***D*****$_R$****-1 in the dark until complete disappearance of* ***D*****$_T$****-1 signals after 60 min. c)* ^{1}*H NMR spectra (*CD_2Cl_2*, 400 MHz, –90 °C) recorded during irradiation of isomer* ***D*****$_R$****-1 with 470 nm light, which leads to photoisomerization to* ***C*****$_R$****-1 until a photoequilibrium of 43%* ***D*****$_R$****-1 and 57%* ***C*****$_R$****-1 is established after 90 min. d)* ^{1}*H VT-NMR spectra (*CD_2Cl_2*, 400 MHz) showing the thermal* ***C*****$_R$****-1 to* ***C*****$_T$****-1 atropisomerization in the dark upon warming from –90 °C (top) to 25 °C (bottom). e)* ^{1}*H NMR spectra (different* CD_2Cl_2*:*CS_2 *ratios, 400 MHz, 23 °C) recorded after addition of* CS_2 *to a solution of* ***C*****$_T$****-1 and* ***C*****$_R$****-1 in* CD_2Cl_2*. First spectrum: Mixture of 29%* ***C*****$_T$****-1 and 71%* ***C*****$_R$****-1 in pure* CD_2Cl_2*. Last spectrum: Mixture of 76%* ***C*****$_T$****-1 and 24%* ***C*****$_R$****-1 in pure* CS_2*.*

When considering the four-step isomer interconversion under illumination in apolar solvents and the associated structural changes, a distinct type of rotary molecular motor behavior is established

https://doi.org/10.26434/chemrxiv-2024-6f898 **ORCID:** https://orcid.org/0000-0002-5055-9924 Content not peer-reviewed by ChemRxiv. **License:** CC BY 4.0

for **1** (Figure 7). However, in this molecular motor directional circular rotation is not proceeding around a specific covalent bond axis. Instead, the PEG-linker chain moves directionally around a shifted virtual axis. To visualize this directional movement, we chose a single marker point on the PEG-chain that can be followed in its position with respect to the fixed thioindigo fragment during operation of motor **1**. In the initial $\mathbf{C_T}$**-1** state, the ethylene glycol chain connecting the indanone rotor to the biaryl unit, reaches from one half-space of the thioindigo plane to the other, thus adopting a S-shape conformation. This positions the chosen marker point on the PEG-linker at the upper right area (position 1) for the chosen perspective in Figure 7. Visible light induced photoisomerization to $\mathbf{D_T}$**-1** is accompanied by severe stretching of the S-shaped PEG-linker, which is also evident from the theoretically obtained geometry. Now the marker point on the PEG-linker resides in the upper left position (position 2 in Figure 7). Upon thermal atropisomerization from $\mathbf{D_T}$**-1** to $\mathbf{D_R}$**-1** the attachment points of the PEG-linker chain reside in the same half-space of the thioindigo plane leading to a relaxed structure. Consequently, the marker point on the linker now resides in the lower left position (position 3 in Figure 7). This atropisomerization represents a thermal ratcheting step enabling the motor to continue directional rotation by entering a second separate photoequilibrium. Isomer $\mathbf{D_R}$**-1** thus photoisomerizes into $\mathbf{C_R}$**-1**, which compresses the PEG-linker chain and shifts the marker point in the lower right position (position 4 in Figure 7). Another thermal ratcheting step atropisomerizes the biaryl axis and repopulates the initial $\mathbf{C_T}$**-1** state. When following the marked point on the PEG-linker chain during one full operational cycle a unidirectional circular rotation trajectory is established proceeding around a virtual axis with respect to the molecule. Although a molecular motor is used with intrinsic directionality for 360° rotation around its double bond axis, this motion is inhibited within the small macrocycle structure. Instead, only 180° of the double bond rotation is accessible, which proceeds exclusively within the bottom half-space of the thioindigo plane (see also Figure 2b for depiction of the half-space assignments). Because this back-and-forth rotation is coupled to thermal atropisomerizations in **1**, symmetry is broken for the motions and directional 360° rotation is established around a new and shifted virtual axis. When comparing the two rotations in the separated HTI-motor component (directional double bond rotation) and corresponding macrocyclic **1** (directional rotation around virtual axis) a reversal of directionality is also observed. While the HTI-motor intrinsically rotates clockwise for the perspective chosen in Figures 1 and 7 macrocyclic motor **1** now rotates counterclockwise instead. The macrocyclization approach therefore enables a precise reprogramming of a molecular motors directional motions without resorting to changing the

https://doi.org/10.26434/chemrxiv-2024-6f898 **ORCID:** https://orcid.org/0000-0002-5055-9924 Content not peer-reviewed by ChemRxiv. **License:** CC BY 4.0

identity of the embedded motor structure itself.[66] We believe that such approach will be of high interest when considering both, design as well as applications of molecular motors in the future.

The second important feature of macrocycle **1** is the possibility for altering its function by simple solvent changes. While in apolar solvents the four-step motor rotation proceeds with up to 79% efficiency, simple two-state photoswitching occurs in polar solvents instead without inherent directionality.

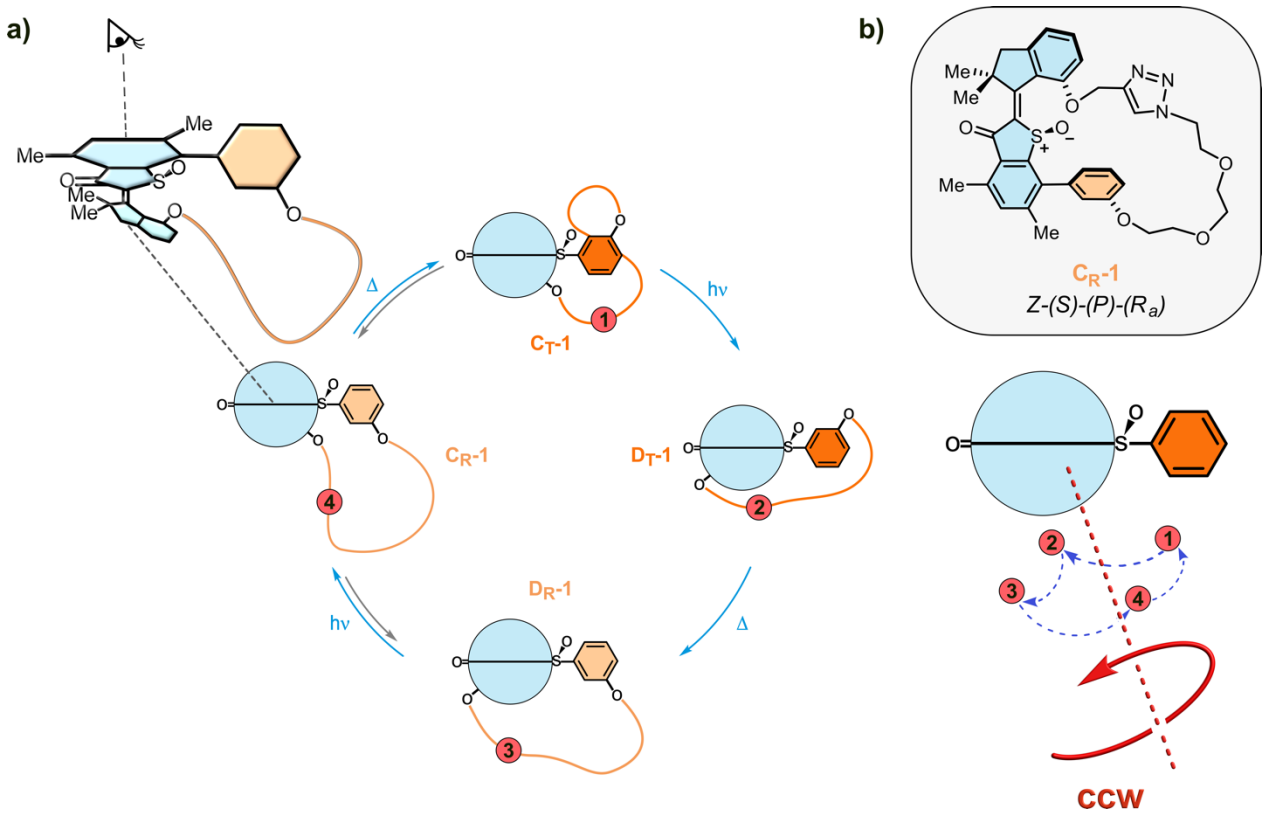

Figure 7 *Unidirectional motor rotation of macrocycle **1**. a) Schematic illustration of the four-step rotational cycle of motor system **1**. Alternating light-triggered photoisomerizations and thermally induced atropisomerizations lead to stretching and compressing of the PEG-linker chain. Observation of a fixed point on the chain allows to follow unidirectional rotation around a virtual rotational axis (red). Atropisomers with (R_a)-configured biaryl and relaxed linker are depicted in light orange, (S_a)-configuration and tensed conformation of the linker is indicated in dark orange. b) Schematic depiction of the unidirectional movement of one specific point on the ethylene glycol linker with position 1 representing the conformation of the chain in **C_T-1**. The molecular structure of **C_R-1** representing position 4 is shown in full detail exemplarily (grey box).*

https://doi.org/10.26434/chemrxiv-2024-6f898 **ORCID:** https://orcid.org/0000-0002-5055-9924 Content not peer-reviewed by ChemRxiv. **License:** CC BY 4.0

In conclusion, we present a concept for reprogramming light driven molecular motors to shift and reverse their intrinsic unidirectional rotations. Using a deliberate macrocyclization strategy opposite directional rotation is established around a virtual axis with respect to the intrinsic directionality of the motor component. Further, simple solvent changes allow to toggle the function of this molecular machine between a four-step molecular motor and a two-step molecular photoswitch reversibly. This sensitivity to the environmental polarity enables a second level of control over molecular machine functions. It can be used to deliberately sense a particular environment, adjust the machines motions accordingly, and allosterically change its behavior. With these results an entry-point for multi-purpose molecular machines and their in-situ programming has been established, which opens up exciting possibilities especially with regard to applications of the same machine for different and even opposing tasks.

Acknowledgement

H. Dube thanks the Deutsche Forschungsgemeinschaft (DFG) for an Emmy Noether fellowship (DU 1414/1-2). This project has also received funding from the European Research Council (ERC) under the European Union's Horizon 2020 research and innovation programme (PHOTOMECH, grant agreement No 101001794). We further thank B. Regen-Pregizer for advising synthesis and data analysis in the beginning of this project.

References

1. Krause, S.; Feringa, B. L., Towards artificial molecular factories from framework-embedded molecular machines. *Nat. Rev. Chem.* **2020,** *4* (10), 550-562.
2. Kassem, S.; van Leeuwen, T.; Lubbe, A. S.; Wilson, M. R.; Feringa, B. L.; Leigh, D. A., Artificial molecular motors. *Chem. Soc. Rev.* **2017,** *46* (9), 2592-2621.
3. Feringa, B. L., The Art of Building Small: From Molecular Switches to Motors (Nobel Lecture). *Angew. Chem. Int. Ed.* **2017,** *56* (37), 11060-11078.
4. Erbas-Cakmak, S.; Leigh, D. A.; McTernan, C. T.; Nussbaumer, A. L., Artificial Molecular Machines. *Chem. Rev.* **2015,** *115* (18), 10081-10206.
5. Feng, Y.; Ovalle, M.; Seale, J. S. W.; Lee, C. K.; Kim, D. J.; Astumian, R. D.; Stoddart, J. F., Molecular Pumps and Motors. *J. Am. Chem. Soc.* **2021,** *143* (15), 5569-5591.
6. Stoddart, J. F., Mechanically Interlocked Molecules (MIMs)-Molecular Shuttles, Switches, and Machines (Nobel Lecture). *Angew. Chem. Int. Ed.* **2017,** *56* (37), 11094-11125.
7. Sauvage, J. P., From Chemical Topology to Molecular Machines (Nobel Lecture). *Angew. Chem. Int. Ed.* **2017,** *56* (37), 11080-11093.

https://doi.org/10.26434/chemrxiv-2024-6f898 **ORCID:** https://orcid.org/0000-0002-5055-9924 Content not peer-reviewed by ChemRxiv. **License:** CC BY 4.0

8. Costil, R.; Holzheimer, M.; Crespi, S.; Simeth, N. A.; Feringa, B. L., Directing Coupled Motion with Light: A Key Step Toward Machine-Like Function. *Chem. Rev.* **2021,** *121* (21), 13213-13237.
9. Balzani, V.; Credi, A.; Venturi, M., *Molecular Devices and Machines—Concepts and Perspectives for the Nanoworld*. Wiley-VCH: 2008.
10. Astumian, R. D., Trajectory and Cycle-Based Thermodynamics and Kinetics of Molecular Machines: The Importance of Microscopic Reversibility. *Acc. Chem. Res.* **2018,** *51* (11), 2653-2661.
11. Borsley, S.; Leigh, D.; Roberts, B. M. W., Molecular Ratchets and Kinetic Asymmetry: Giving Chemistry Direction. *Angew. Chem. Int. Ed.* **2024**, e202400495.
12. Pooler, D. R. S.; Lubbe, A. S.; Crespi, S.; Feringa, B. L., Designing light-driven rotary molecular motors. *Chem. Sci.* **2021,** *12* (45), 14964-14986.
13. Roke, D.; Wezenberg, S. J.; Feringa, B. L., Molecular rotary motors: Unidirectional motion around double bonds. *Proc. Natl. Acad. Sci. U. S. A.* **2018,** *115* (38), 9423-9431.
14. Corra, S.; Curcio, M.; Credi, A., Photoactivated Artificial Molecular Motors. *JACS Au* **2023,** *3* (5), 1301-1313.
15. Baroncini, M.; Silvi, S.; Credi, A., Photo- and Redox-Driven Artificial Molecular Motors. *Chem. Rev.* **2020,** *120*, 200-268.
16. Garcia-Lopez, V.; Liu, D.; Tour, J. M., Light-Activated Organic Molecular Motors and Their Applications. *Chem. Rev.* **2020,** *120* (1), 79-124.
17. Michl, J.; Sykes, E. C. H., Molecular Rotors and Motors: Recent Advances and Future Challenges. *ACS Nano* **2009,** *3*, 1042-1048.
18. Koumura, N.; Zijlstra, R. W. J.; van Delden, R. A.; Feringa, B. L., Light-driven monodirectional molecular rotor. *Nature* **1999,** *401* (6749), 152-155.
19. Hernandez, J. V.; Kay, E. R.; Leigh, D. A., A Reversible Synthetic Rotary Molecular Motor. *Science* **2004,** *306*, 1532-1537.
20. Wilson, M. R.; Sola, J.; Carlone, A.; Goldup, S. M.; Lebrasseur, N.; Leigh, D. A., An autonomous chemically fuelled small-molecule motor. *Nature* **2016,** *534* (7606), 235-240.
21. Erbas-Cakmak, S.; Fielden, S. D. P.; Karaca, U.; Leigh, D. A.; McTernan, C. T.; Tetlow, D. J.; Wilson, M. R., Rotary and linear molecular motors driven by pulses of a chemical fuel. *Science* **2017,** *358* (6361), 340-343.
22. Borsley, S.; Kreidt, E.; Leigh, D. A.; Roberts, B. M. W., Autonomous fuelled directional rotation about a covalent single bond. *Nature* **2022,** *604* (7904), 80-85.
23. Fletcher, S. P.; Dumur, F.; Pollard, M. M.; Feringa, B. L., A Reversible, Unidirectional Molecular Rotary Motor Driven by Chemical Energy. *Science* **2005,** *310*, 80-82.
24. Collins, B. S. L.; Kistemaker, J. C. M.; Otten, E.; Feringa, B. L., A chemically powered unidirectional rotary molecular motor based on a palladium redox cycle. *Nat. Chem.* **2016,** *8* (9), 860-866.
25. Tierney, H. L.; Murphy, C. J.; Jewell, A. D.; Baber, A. E.; Iski, E. V.; Khodaverdian, H. Y.; McGuire, A. F.; Klebanov, N.; Sykes, E. C. H., Experimental demonstration of a single-molecule electric motor. *Nat. Nanotechnol.* **2011,** *6*, 625-629.
26. Perera, U. G. E.; Ample, F.; Kersell, H.; Zhang, Y.; Vives, G.; Echeverria, J.; Grisolia, M.; Rapenne, G.; Joachim, C.; Hla, S.-W., Controlled clockwise and anticlockwise rotational switching of a molecular motor. *Nat. Nanotechnol.* **2013,** *8*, 46-51.
27. Zhang, L.; Qiu, Y.; Liu, W. G.; Chen, H.; Shen, D.; Song, B.; Cai, K.; Wu, H.; Jiao, Y.; Feng, Y.; Seale, J. S. W.; Pezzato, C.; Tian, J.; Tan, Y.; Chen, X. Y.; Guo, Q. H.; Stern, C. L.; Philp, D.; Astumian, R. D.; Goddard, W. A., 3rd; Stoddart, J. F., An electric molecular motor. *Nature* **2023,** *613* (7943), 280-286.

https://doi.org/10.26434/chemrxiv-2024-6f898 **ORCID:** https://orcid.org/0000-0002-5055-9924 Content not peer-reviewed by ChemRxiv. **License:** CC BY 4.0

28. Barrell, M. J.; Campana, A. G.; von Delius, M.; Geertsema, E. M.; Leigh, D. A., Light-driven transport of a molecular walker in either direction along a molecular track. *Angew. Chem. Int. Ed.* **2011,** *50* (1), 285-290.
29. von Delius, M.; Geertsema, E. M.; Leigh, D. A., A synthetic small molecule that can walk down a track. *Nat. Chem.* **2010,** *2*, 96-101.
30. Ragazzon, G.; Baroncini, M.; Silvi, S.; Venturi, M.; Credi, A., Light-powered autonomous and directional molecular motion of a dissipative self-assembling system. *Nat. Nanotechnol.* **2015,** *10*, 70-75.
31. Corra, S.; Bakic, M. T.; Groppi, J.; Baroncini, M.; Silvi, S.; Penocchio, E.; Esposito, M.; Credi, A., Kinetic and energetic insights into the dissipative non-equilibrium operation of an autonomous light-powered supramolecular pump. *Nat. Nanotechnol.* **2022,** *17* (7), 746-751.
32. Qiu, Y.; Song, B.; Pezzato, C.; Shen, D.; Liu, W.; Zhang, L.; Feng, Y.; Guo, Q.-H.; Cai, K.; Li, W.; Chen, H.; Nguyen, M. T.; Shi, Y.; Cheng, C.; Astumian, R. D.; Li, X.; Stoddart, J. F., A precise polyrotaxane synthesizer. *Science* **2020,** *368* (6496), 1247-1253.
33. Cheng, C.; McGonigal, P. R.; Schneebeli, S. T.; Li, H.; Vermeulen, N. A.; Ke, C.; Stoddart, J. F., An artificial molecular pump. *Nat. Nanotechnol.* **2015,** *10* (6), 547-553.
34. Thomas, D.; Tetlow, D. J.; Ren, Y.; Kassem, S.; Karaca, U.; Leigh, D. A., Pumping between phases with a pulsed-fuel molecular ratchet. *Nat. Nanotechnol.* **2022,** *17* (7), 701-707.
35. Amano, S.; Fielden, S. D. P.; Leigh, D. A., A catalysis-driven artificial molecular pump. *Nature* **2021,** *594* (7864), 529-534.
36. Bhosale, S.; Sisson, A. L.; Talukdar, P.; Fürstenberg, A.; Banerji, N.; Vauthey, E.; Bollot, G.; Mareda, J.; Röger, C.; Würthner, F.; Sakai, N.; Matile, S., Photoproduction of proton gradients with pi-stacked fluorophore scaffolds in lipid bilayers. *Science* **2006,** *313* (5783), 84-6.
37. Koumura, N.; Geertsema, E. M.; van Gelder, M. B.; Meetsma, A.; Feringa, B. L., Second Generation Light-Driven Molecular Motors. Unidirectional Rotation Controlled by a Single Stereogenic Center with Near-Perfect Photoequilibria and Acceleration of the Speed of Rotation by Structural Modification. *J. Am. Chem. Soc.* **2002,** *124* (18), 5037-5051.
38. Kistemaker, H. A.; Stacko, P.; Visser, J.; Feringa, B. L., Unidirectional rotary motion in achiral molecular motors. *Nat. Chem.* **2015,** *7* (11), 890-896.
39. Greb, L.; Lehn, J. M., Light-driven molecular motors: imines as four-step or two-step u nidirectional rotors. *J. Am. Chem. Soc.* **2014,** *136* (38), 13114-13117.
40. Greb, L.; Eichhofer, A.; Lehn, J. M., Synthetic Molecular Motors: Thermal N Inversion and Directional Photoinduced CN Bond Rotation of Camphorquinone Imines. *Angew. Chem. Int. Ed.* **2015,** *54*, 14345–14348.
41. Guentner, M.; Schildhauer, M.; Thumser, S.; Mayer, P.; Stephenson, D.; Mayer, P. J.; Dube, H., Sunlight-powered kHz rotation of a hemithioindigo-based molecular motor. *Nat. Commun.* **2015,** *6* (1), 8406.
42. Huber, L. A.; Hoffmann, K.; Thumser, S.; Böcher, N.; Mayer, P.; Dube, H., Direct Observation of Hemithioindigo-Motor Unidirectionality. *Angew. Chem. Int. Ed.* **2017,** *56* (46), 14536-14539.
43. Wilcken, R.; Schildhauer, M.; Rott, F.; Huber, L. A.; Guentner, M.; Thumser, S.; Hoffmann, K.; Oesterling, S.; de Vivie-Riedle, R.; Riedle, E.; Dube, H., Complete Mechanism of Hemithioindigo Motor Rotation. *J. Am. Chem. Soc.* **2018,** *140* (15), 5311-5318.

https://doi.org/10.26434/chemrxiv-2024-6f898 **ORCID:** https://orcid.org/0000-0002-5055-9924 Content not peer-reviewed by ChemRxiv. **License:** CC BY 4.0

44. Gerwien, A.; Mayer, P.; Dube, H., Photon-Only Molecular Motor with Reverse Temperature-Dependent Efficiency. *J. Am. Chem. Soc.* **2018,** *140* (48), 16442-16445.
45. Gerwien, A.; Mayer, P.; Dube, H., Green light powered molecular state motor enabling eight-shaped unidirectional rotation. *Nat. Commun.* **2019,** *10* (1), 4449.
46. Huber, L. A.; Thumser, S.; Grill, K.; Vossiek, D.; Bach, N. N.; Mayer, P.; Dube, H., Steric Effects on the Thermal Processes of Hemithioindigo Based Molecular Motor Rotation. *Chem. Eur. J.* **2021,** *27* (41), 10758-10765.
47. Wilcken, R.; Huber, L.; Grill, K.; Guentner, M.; Schildhauer, M.; Thumser, S.; Riedle, E.; Dube, H., Tuning the Ground and Excited State Dynamics of Hemithioindigo Molecular Motors by Changing Substituents. *Chem. Eur. J.* **2020,** *26* (59), 13507-13512.
48. Schildhauer, M.; Rott, F.; Thumser, S.; Mayer, P.; de Vivie-Riedle, R.; Dube, H., A Prospective Ultrafast Hemithioindigo Molecular Motor. *ChemPhotoChem* **2019,** *3*, 365-371.
49. Schapiro, I.; Gueye, M.; Paolino, M.; Fusi, S.; Marchand, G.; Haacke, S.; Martin, M. E.; Huntress, M.; Vysotskiy, V. P.; Veryazov, V.; Leonard, J.; Olivucci, M., Synthesis, spectroscopy and QM/MM simulations of a biomimetic ultrafast light-driven molecular motor. *Photochem. Photobiol. Sci.* **2019,** *18* (9), 2259-2269.
50. Kuntze, K.; Pooler, D. R. S.; Di Donato, M.; Hilbers, M. F.; van der Meulen, P.; Buma, W. J.; Priimagi, A.; Feringa, B. L.; Crespi, S., A visible-light-driven molecular motor based on barbituric acid. *Chem. Sci.* **2023,** *14* (32), 8458-8465.
51. Roke, D.; Sen, M.; Danowski, W.; Wezenberg, S. J.; Feringa, B. L., Visible-Light-Driven Tunable Molecular Motors Based on Oxindole. *J. Am. Chem. Soc.* **2019,** *141* (18), 7622-7627.
52. Ryabchun, A.; Lancia, F.; Chen, J.; Plamont, R.; Morozov, D.; Feringa, B. L.; Katsonis, N., Macroscopic motion from synchronized molecular power strokes. *Chem* **2023,** *9* (12), 3544-3554.
53. Li, Q.; Fuks, G.; Moulin, E.; Maaloum, M.; Rawiso, M.; Kulic, I.; Foy, J. T.; Giuseppone, N., Macroscopic contraction of a gel induced by the integrated motion of light-driven molecular motors. *Nat. Nanotechnol.* **2015,** *10*, 161-165.
54. Foy, J. T.; Li, Q.; Goujon, A.; Colard-Itte, J.-R.; Fuks, G.; Moulin, E.; Schiffmann, O.; Dattler, D.; Funeriu, D. P.; Giuseppone, N., Dual-light control of nanomachines that integrate motor and modulator subunits. *Nat. Nanotechnol.* **2017,** *12*, 540-545.
55. Uhl, E.; Thumser, S.; Mayer, P.; Dube, H., Transmission of Unidirectional Molecular Motor Rotation to a Remote Biaryl Axis. *Angew. Chem. Int. Ed.* **2018,** *57*, 11064-11068.
56. Uhl, E.; Mayer, P.; Dube, H., Active and Unidirectional Acceleration of Biaryl Rotation by a Molecular Motor. *Angew. Chem. Int. Ed.* **2020,** *59* (14), 5730-5737.
57. Kathan, M.; Crespi, S.; Troncossi, A.; Stindt, C. N.; Toyoda, R.; Feringa, B. L., The Influence of Strain on the Rotation of an Artificial Molecular Motor. *Angew. Chem. Int. Ed.* **2022,** *61* (34), e202205801.
58. Gao, C.; Vargas Jentzsch, A.; Moulin, E.; Giuseppone, N., Light-Driven Molecular Whirligig. *J. Am. Chem. Soc.* **2022,** *144* (22), 9845-9852.
59. Kathan, M.; Crespi, S.; Thiel, N. O.; Stares, D. L.; Morsa, D.; de Boer, J.; Pacella, G.; van den Enk, T.; Kobauri, P.; Portale, G.; Schalley, C. A.; Feringa, B. L., A light-fuelled nanoratchet shifts a coupled chemical equilibrium. *Nat. Nanotechnol.* **2022,** *17*, 159-165.
60. Bach, N. N.; Josef, V.; Maid, H.; Dube, H., Active Mechanical Threading by a Molecular Motor. *Angew. Chem. Int. Ed.* **2022,** *61* (19), e202201882.
61. Regen-Pregizer, B. L.; Ozcelik, A.; Mayer, P.; Hampel, F.; Dube, H., A photochemical method to evidence directional molecular motions. *Nat. Commun.* **2023,** *14* (1), 4595.

https://doi.org/10.26434/chemrxiv-2024-6f898 **ORCID:** https://orcid.org/0000-0002-5055-9924 Content not peer-reviewed by ChemRxiv. **License:** CC BY 4.0

62. Regen-Pregizer, B. L.; Dube, H., Defining Unidirectional Motions and Structural Reconfiguration in a Macrocyclic Molecular Motor. *J. Am. Chem. Soc.* **2023,** *145* (24), 13081-13088.
63. Haberhauer, G., A molecular four-stroke motor. *Angew. Chem. Int. Ed.* **2011,** *50* (28), 6415-6418.
64. Hoops, S.; Sahle, S.; Gauges, R.; Lee, C.; Pahle, J.; Simus, N.; Singhal, M.; Xu, L.; Mendes, P.; Kummer, U., COPASI--a COmplex PAthway SImulator. *Bioinformatics* **2006,** *22* (24), 3067-74.
65. Pfeifer, L.; Crespi, S.; van der Meulen, P.; Kemmink, J.; Scheek, R. M.; Hilbers, M. F.; Buma, W. J.; Feringa, B. L., Controlling forward and backward rotary molecular motion on demand. *Nat. Commun.* **2022,** *13* (1), 2124.
66. Ruangsupapichat, N.; Pollard, M. M.; Harutyunyan, S. R.; Feringa, B. L., Reversing the direction in a light-driven rotary molecular motor. *Nat. Chem.* **2010,** *3*, 53-60.

https://doi.org/10.26434/chemrxiv-2024-6f898 **ORCID:** https://orcid.org/0000-0002-5055-9924 Content not peer-reviewed by ChemRxiv. **License:** CC BY 4.0